Energy Dissipation of P- and S-Waves in Fluid-Saturated Rocks: An Overview Focusing on Hydraulically Connected Fractures

J. Germán Rubino[1], **Beatriz Quintal**[1], **Tobias M. Müller**[2], **Luis Guarracino**[3], **Ralf Jänicke**[4],
Holger Steeb[4], **Klaus Holliger***[1]

1. *Applied and Environmental Geophysics Group, Institute of Earth Sciences, University of Lausanne, Lausanne CH 1015, Switzerland*
2. *Energy Flagship, Commonwealth Scientific and Industrial Research Organization, Perth 6000, Australia*
3. *CONICET, Facultad de Ciencias Astronómicasy Geofísicas, Universidad Nacional de La Plata, La Plata B1900, Argentina*
4. *Institute of Mechanics, University of Bochum, Bochum 44787, Germany*

ABSTRACT: An important characteristic of fractured rocks is their high seismic attenuation, which so far has been mainly attributed to wave-induced fluid flow (WIFF) between the fractures and the embedding matrix. The influence of fracture connectivity on seismic attenuation has, however, recently, only been investigated. Numerical compressibility and shear tests based on Biot's quasi-static poro-elastic equations illustrate that an important manifestation of WIFF arises in the presence of fracture connectivity. The corresponding energy loss, which can be significant for both P- and S-waves, is mainly due to fluid flow within the connected fractures and is sensitive to the permeabilities as well as the lengths and intersection angles of the fractures. Correspondingly, this phenomenon contains valuable information on the governing hydraulic properties of fractured rocks and hence should be accounted for whenever realistic seismic models of such media are needed.
KEY WORDS: fractured rocks, seismic attenuation, WIFF, fracture connectivity, embedding matrix, Biot's theory.

0 INTRODUCTION

Fractures are common in most geological formations and tend to dominate their mechanical and hydraulic properties. Correspondingly, there is great interest in improving techniques to detect and characterize both individual fractures as well as fracture networks (e.g., Maultzsch et al., 2003; Nelson, 2001). Since in most cases the resolution of seismic data is not sufficient to directly image fractures, most related research efforts focus on seismic attribute analysis (e.g., Bakulin et al., 2000). Correspondingly, various attributes, such as, for example, shear wave splitting and azimuthal variations in attenuation and phase velocity, have been identified as diagnostic features that may permit to estimate some of the key properties of fractured rocks, such as the density, average size, and orientation of the fractures (e.g., Clark et al., 2009; Maultzsch et al., 2003).

Notably, seismic attenuation has been recognized as a potentially important parameter for studying fractured rock masses, as both laboratory studies and field measurements have shown that seismic energy loss is very significant in fractured media and tends to increase with increasing fracture density (e.g.,

Clark et al., 2009; Maultzsch et al., 2003; Holliger and Bühnmann, 1996; Peacock et al., 1994). Up till now, the strong seismic attenuation typically observed in fractured materials has been considered to be produced by wave-induced fluid flow (WIFF) between the fractures and the pore space of the embedding matrix (e.g., Brajanovski et al., 2005; Chapman, 2003; Peacock et al., 1994). That is, due to the very high compressibility contrast between the fractures and their embedding matrix, seismic waves induce strong local fluid pressure gradients and associated fluid flow, which in turn results in significant attenuation (e.g., Brajanovski et al., 2005). As this fluid pressure equilibration process is largely controlled by the prevailing hydraulic properties, one can expect the observed energy dissipation to also contain information on fracture connectivity, which controls the flow and transport properties of fractured formations (e.g., Berkowitz et al., 2000). Until recently, the effects of fracture connectivity on seismic attenuation did, however, remain largely unexplored, which is likely due to the corresponding limitations of commonly employed effective medium models (e.g., Brajanovski et al., 2005; Chapman, 2003).

In the following, we present an overview of recent studies of this topic (Quintal et al., 2014; Rubino et al., 2014, 2013) and discuss the effects of fracture connectivity on seismic attenuation. To this end, we use a numerical upscaling procedure, which enables us to estimate energy dissipation due to WIFF in complex fractured media and, thus, to study the effects of fracture connectivity on seismic attenuation.

*Corresponding author: klaus.holliger@unil.ch

1 METHODOLOGY

The seismic response of fractured rocks can be modeled using Biot's theory of poro-elasticity (Biot, 1962, 1941), with the fractures represented as highly compliant regions of very high porosity and permeability embedded in a stiffer, less porous and less permeable matrix (e.g., Brajanovski et al., 2005). When a seismic wave is incident on a mesoscale fracture fluid flow is induced from the fracture into the pore space of the embedding matrix and vice versa, which leads to energy loss. Quantifying attenuation due to WIFF at mesoscopic scales, that is, at scales much smaller than the predominant seismic wavelengths but much larger than the typical pore or grain size, is, however, problematic. This is mainly due to the fact that, in the low-frequency range, the diffusion process associated with the fluid pressure equilibration occurs at a very different time scale compared to the wave propagation process. Additional complications arise because the corresponding diffusion lengths are very small compared with the prevailing seismic wavelengths. To overcome these problems, we employ the numerical upscaling procedure presented by Rubino et al. (2009) to estimate the attenuation and velocity dispersion of P- and S-waves due to WIFF.

For the P-wave case, we apply a time-harmonic compression at the top boundary of a two-dimensional rectangular poroelastic medium containing mesoscale fractures. The fluid is not allowed to flow into the sample or out of it. Moreover, no tangential forces are applied on the boundaries of the sample and the solid is neither allowed to move on the bottom boundary nor to have horizontal displacements on the lateral boundaries. The corresponding numerical procedure is based on a finite-element solution of Biot's consolidation equations (Biot, 1941) in the space-frequency domain under appropriate boundary conditions. The equivalent undrained complex plane-wave modulus is expressed in terms of the applied time-harmonic compression and the resulting complex oscillatory volume change. From this parameter we can then derive the desired information regarding the WIFF-related P-wave attenuation and velocity dispersion. Given the ever increasing importance of S-waves in seismic exploration, we also carry out corresponding numerical upscaling experiments based on quasi-static shear, rather than compression, tests. For these numerical experiments, periodic boundary conditions were employed (Jänicke et al., 2015; Quintal et al., 2014). The corresponding numerical procedure is again based on a finite-element solution of Biot's consolidation equations (Biot, 1941), as previously outlined for the P-wave case, but in the space-time rather than in the space-frequency domain (Quintal et al., 2011).

2 RESULTS

2.1 P-Wave Attenuation in Fractured Rocks

Figure 1 shows three rock samples used to explore P-wave attenuation and velocity dispersion in fractured media. We consider a water-saturated quartz sandstone permeated by mesoscale fractures, which are either unconnected or interconnected. The solid grain properties of the fractures are assumed to be the same as those of the background and to correspond to those of quartz. The elastic properties of the fractures are estimated following the approach proposed by Nakagawa and
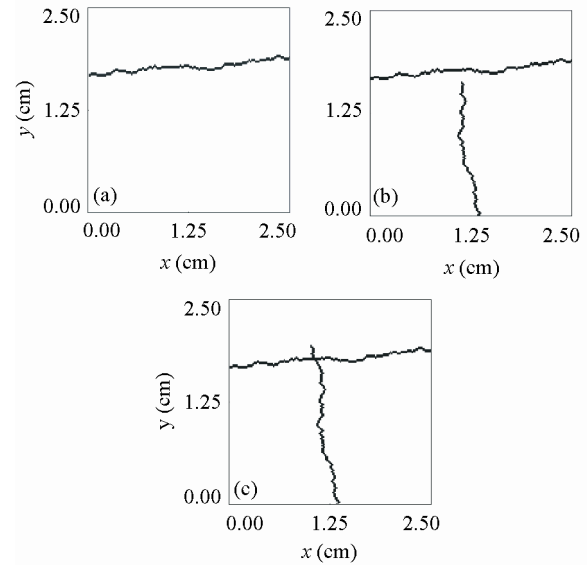
Figure 1. Synthetic rock samples used to analyze fracture connectivity effects on P-wave attenuation and velocity dispersion. Fractures are denoted by solid "wiggly" lines (modified after Rubino et al. (2013)).

Table 1 Rock physical properties used for studying the attenuation of P-waves in fractured media. Adopted from Rubino et al. (2013)

Parameter	Embedding matrix	Fractures
Bulk modulus of the grains	37 GPa	37 GPa
Shear modulus of the grains	44 GPa	44 GPa
Density of the grains	2 650 kg/m^3	2 650 kg/m^3
Bulk modulus of the dry frame	23 GPa	0.02 GPa
Shear modulus of the dry frame	27 GPa	0.01 GPa
Porosity	0.1	0.5
Permeability	23 mD	100 mD

Schoenberg (2007). Table 1 provides a summary of the elastic properties of the grains and the dry-frame. The shear viscosity and the bulk modulus of the pore water are 3.0 mPa · s and 2.25 GPa, respectively.
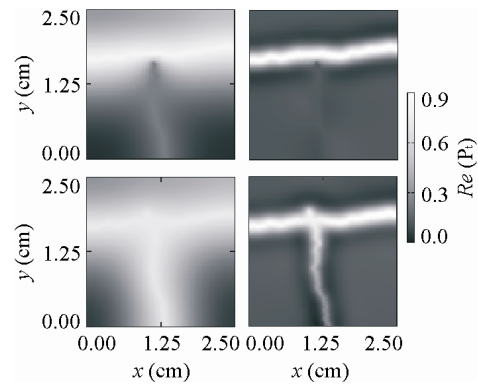
The samples are characterized by a homogeneous background embedding one sub-horizontal fracture (Fig. 1a), one sub-horizontal and one non-intersecting sub-vertical fracture (Fig. 1b), and one sub-horizontal fracture and one intersecting sub-vertical fracture (Fig. 1c). The mean aperture of the fractures is 0.33 mm. The inverse quality factors of vertically propagating P-waves are displayed in Fig. 2. The dashed curve in the top panel indicates that the presence of fractures perpendicular to the direction of wave propagation produces very strong attenuation over a wide range of frequencies. This is expected, because the strong compressibility contrast between fracture and its embedding matrix produces a significant amount of fluid flow between these regions in response to the applied stresses. By comparing the dashed and solid curves we see that adding a non-intersecting fracture parallel to the direction of wave propagation does not affect the attenuation significantly. This is again expected, since the stress applied to the sample does not change significantly the fluid pressure in the
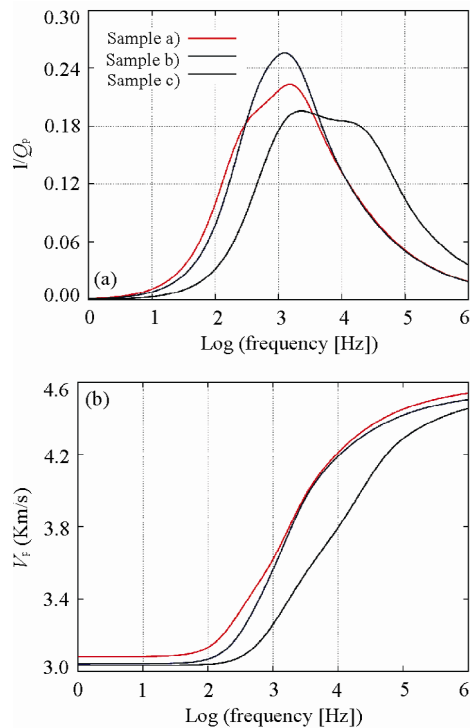
Figure 2. (a) Attenuation, as quantified by the inverse quality factor $1/Q_p$, and (b) phase velocity for vertically propagating P-waves as functions of frequency for the rock samples shown in Fig. 1 (modified after Rubino et al. (2013)).

Figure 3. Real part of fluid pressure normalized with respect to the amplitude of the stress applied along the upper boundary of the sample. Top panels correspond to the sample shown in Fig. 1b where the sub-horizontal and sub-vertical fractures do not intersect, while bottom ones correspond to sample shown in Fig. 1c where the sub-horizontal and sub-vertical do intersect. Left panels correspond to a frequency of 1.3 kHz, while right ones to 29 kHz (modified after Rubino et al. (2013)).

sub-vertical fracture and, hence, there are no significant WIFF effects. However, as the sub-vertical fracture intersects the sub-horizontal one (dotted lines), significant changes in the overall attenuation and phase velocity arise. We observe that the maximum attenuation decreases slightly and that the frequency range where this parameter is relevant broadens. Moreover, there are two local maxima at 1.3 and 29 kHz. The first attenuation peak occurs at a frequency similar to that of the peaks of the solid and dashed lines, thus indicating that it may be due to fluid exchange between the sub-horizontal fracture and the embedding matrix. Conversely, the presence of a second attenuation peak at higher frequencies may be indicative of an additional energy dissipation phenomenon related to the intersection of the two fractures. The corresponding velocity dispersion curves are shown in Fig. 2. A velocity difference of up to 10% can be observed when comparing the connected and unconnected scenarios between 1 and 50 kHz.

In order to study the physical nature of the second attenuation peak, we show in Fig. 3 the real part of the fluid pressure field normalized with respect to the amplitude of the stress applied on the top boundary of the sample. We observe in the top left panel that the applied compression produces a significant fluid pressure increase in the highly compliant sub-horizontal fracture as compared to the stiffer background rock. The fluid pressure gradient induces significant fluid flow across the boundary of fracture and background rock and, hence, attenuation. This is illustrated by the solid curve in Fig. 2. It is also interesting to notice that the fluid pressure induced within the sub-vertical fracture is relatively low so that its presence does not change significantly the fluid pressure field throughout the

sample. However, when the sub-vertical fracture intersects the sub-horizontal one, the fluid pressure field changes rather dramatically, as illustrated by the bottom left-panel of Fig. 3. We observe that the fluid pressure in the sub-vertical fracture increases significantly while the sub-horizontal fracture experiences a slight fluid pressure reduction as compared to the unconnected scenario. Correspondingly, the amount of fluid flow between the sub-horizontal fracture and the embedding matrix decreases. Fluid flow between the fractures and the embedding matrix also takes place in the vicinity of the sub-vertical fracture, albeit at a less significant level. These changes in the WIFF pattern have corresponding effects on the attenuation (Fig. 2). For the frequency at which the second attenuation peak occurs, fluid pressure changes in the background rock are limited to the immediate vicinity of the fractures, as illustrated by the panels on the right-hand side of Fig. 3. This is expected because the corresponding diffusion lengths become smaller as the frequency increases. Accordingly, fluid exchange between the sub-horizontal fracture and the background rock is much less significant for this higher frequency. Again, the presence of the sub-vertical fracture does not modify significantly the fluid pressure field when there is no connection. However, as soon as the fractures intersect, the fluid pressure field changes substantially, as evidenced by the comparison of the top and bottom right panels of Fig. 3. Interestingly, for this higher frequency there is a significant fluid pressure gradient and corresponding fluid flow inside the sub-vertical fracture. This fluid is injected from the sub-horizontal fracture, which experiences a fluid pressure increase in response to the applied compression. Therefore, while fluid flow within the sub-horizontal fracture is not very significant when there is no fracture intersection, it also becomes substantial when there is fracture intersection.

These results show that at the frequency of the second attenuation peak WIFF is much more significant in the presence of connected fractures and occurs predominantly within the fractures, which in turn makes this phenomenon the most likely explanation of the corresponding additional attenuation peak.

To confirm this hypothesis, we decreased the permeability of the embedding matrix by three orders-of-magnitude and recomputed the resulting attenuation curve. Attenuation peaks associated with fluid flow in the background should then shift towards lower frequencies, as the corresponding transition frequency is directly proportional to the permeability of the embedding matrix, while those produced by fluid flow within fractures should remain unchanged. The corresponding results, which are not shown here for brevity, confirm that when there is no fracture connection the attenuation peak moves towards lower frequencies when decreasing the permeability of the embedding matrix. In the presence of fracture connectivity, the peak originally located at a frequency 1.3 kHz also shifts towards lower frequencies, whereas the one located at 29 kHz remains at the same location. All this clearly demonstrates that the second attenuation peak is not a result of fluid flow between the fractures and the embedding matrix, but rather related to fluid flow within the fractures.

2.2 S-Wave Attenuation in Fractured Rocks

So far, we have focused our attention on the attenuation of P-waves. For the corresponding analyses of S-waves, the models measure 10×10 cm and contain fractures in two orientations (Fig. 4). The fractures are again modeled as poro-elastic features that are much more compressible and have a much higher porosity and permeability than the embedding matrix, which is assumed to correspond to tight quartz sandstone (Table 2). The saturating pore water has a viscosity of 1.0 mPa·s^{-1} and a bulk modulus of 2.4 GPa. The fractures have an aperture of 0.1 mm. The shape of the fracture inclined at 45° in Fig. 4 is an ellipse, while the horizontal fracture crossing the whole sample in the connected case is rectangular. In the unconnected case, each of the horizontal fractures has a rectangular extremity at the sample boundary and an elliptical extremity within the sample.

Figure 5 shows the results of the numerical shear test applied to the samples shown in Fig. 4 (Quintal et al., 2014). For the unconnected scenario, the S-wave attenuation peaks at a frequency 3.2 Hz (red dashed line), while for the connected scenario (red solid line) an additional peak arises at 191 Hz. In the latter case, the first attenuation peak at 3.2 Hz is still present, but its magnitude is much smaller than in the unconnected scenario. This finding is consistent with the corresponding results obtained for the attenuation of P-waves (Figs. 1 and 2). Here, the attenuation peak at lower frequencies was related to fluid flow in the embedding matrix, while the peak at higher frequencies was related to fluid flow through the fractures (Fig. 2a). To explore whether the two attenuation peaks observed for S-wave attenuation in Fig. 5 are also predominantly associated with these two different flow phenomena, the permeability of the embedding matrix was decreased from 0.1 mD first to 0.05 mD and then to 0.025 mD while keeping the fracture permeability unchanged (Table 2). The corresponding results shown in Fig. 5 illustrate that a decrease in permeability of the matrix embedding the fractures causes (i) a shift of the attenuation peak located at lower frequencies to even lower frequencies, for both the connected and unconnected scenarios, and (ii) no change at all for the attenuation peak located at higher frequencies that is present for the connected fractures. This demonstrates that the
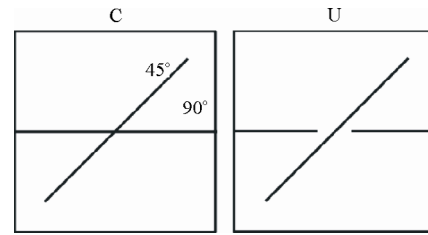
Figure 4. Models of pairs of connected (C) and unconnected (U) fractures. Each model corresponds to a synthetic rock sample measuring 10×10 cm. The fracture aperture is 0.1 mm (modified after Quintal et al. (2014)).

Table 2 Rock physical properties used for studying the attenuation of S-waves in fractured media. Adopted from Quintal et al. (2014)

| Parameter	Embedding matrix	Fractures
Bulk modulus of the grains	40 GPa	40 GPa
Shear modulus of the grains	44 GPa	44 GPa
Density of the grains	2 650 kg/m^3	2 650 kg/m^3
Bulk modulus of the dry frame	34 GPa	0.025 GPa
Shear modulus of the dry frame	32 GPa	0.020 GPa
Porosity	0.06	0.5
Permeability	0.1 mD	10 mD
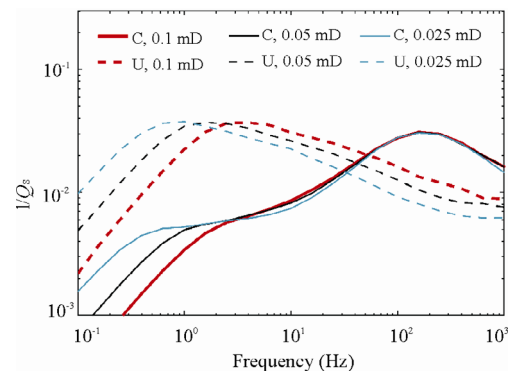
Figure 5. S-wave attenuation, $1/Q_S$, for the connected (C) and unconnected (U) fracture models shown in Fig. 4 for a range of permeabilities of the embedding matrix as indicated in the legend (modified after Quintal et al. (2014)).

S-wave attenuation peak at lower frequencies is indeed influenced by fluid flow in the embedding matrix, while the additional peak observed at higher frequencies in the presence of connected fractures is not. This implies that in the latter case attenuation must be dominated by fluid flow through the connected fractures, which in turn suggests that the two different P-wave attenuation peaks prevailing in fractured media in presence of fracture connectivity (Fig. 2) find their corresponding expressions in the attenuation behavior of S-waves (Fig. 5).

In an effort to better understand the inferred S-wave attenuation characteristics (Fig. 5), we took snapshots of the fluid pressure (Fig. 6) and the fluid velocity (Fig. 7) during shear tests applied to the samples of the type shown in Fig. 4. Please note that, for visualization purposes, the fractures used to calculate these snapshots have a five times larger aperture, that is, 0.5 mm instead of 0.1 mm, than those used in the original shear
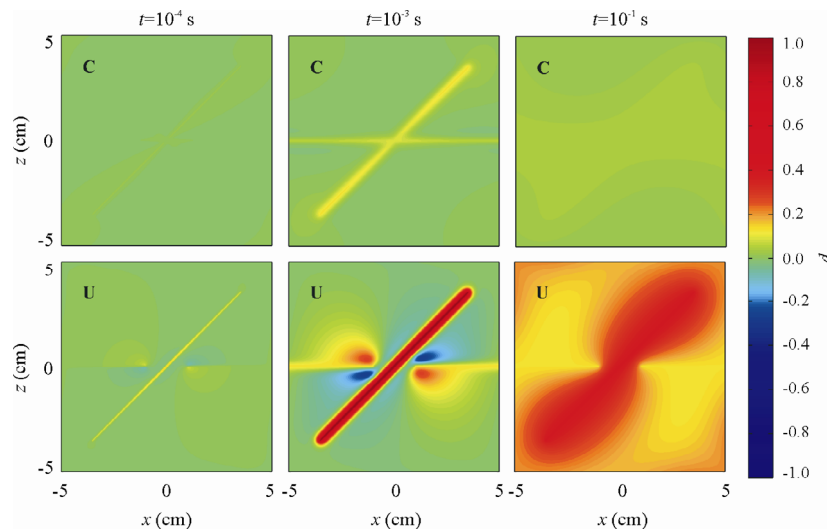
Figure 6. Snapshots of the fluid pressure P, normalized with respect to its maximum value. The models are similar to the ones shown in Fig. 4, but with fractures being five times thicker for visualization purposes. On the top-left of each snapshot, C and U refer to connected and unconnected scenarios, respectively. The total simulated time was 1 s and, to simulate the shear test, the displacements at the boundaries were an approximate step function. This approximate step function was rapidly increased from 0 to its maximum value between the times 0 and 5×10^{-4} s.
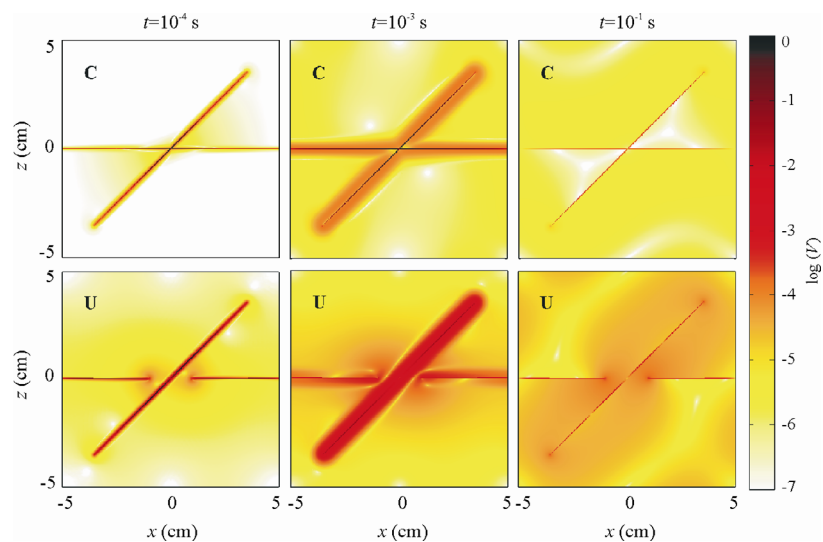
Figure 7. Snapshots of the modulus of fluid velocity V, normalized with respect to its maximum value. The models are similar to the ones shown in Fig. 4, but with fractures being five times thicker for visualization purposes. On the top-left of each snapshot, C and U refer to connected and unconnected scenarios, respectively. The total simulation time was 1 s and, to perform the shear test, the displacement at the boundaries was an approximate step function, which was ramped up to its maximum value between within the initial 5×10^{-4} s.

tests. We observe that in the connected scenario the induced pressure differences are very rapidly equilibrated due to the preferential flow path that the fluid encounters via the interconnected fractures. Conversely, the scenario involving unconnected fractures lacks such a preferential flow path, which in turn results in slow equilibration of the pressure differences. Additionally, pressure gradients within the embedding matrix can be observed for this case, which result in fluid flowing predominantly from the fractures into the embedding matrix. The low permeability of the embedding matrix makes this process much slower than that in the connected case, where fluid flow is dominated by the high permeability of the interconnected frac-

tures, and hence most of attenuation occurs at lower frequencies in the unconnected scenario (Figs. 5, 6, and 7).

S-wave attenuation in the considered fractured rock models is caused by the flow of the viscous pore fluid. This might seem counter-intuitive at first glance as fluids cannot support any shear stresses. However, fluids can support compression and extension. In presence of heterogeneities, the boundary conditions associated with shear experiments do indeed locally lead to compressional and extensional stress regimes (Quintal et al., 2012), which in turn result in corresponding local variations in fluid pressure (Berryman and Wang, 2001). The fluid pressure differences illustrated in the snapshots shown in Fig. 6 are

thus a direct consequence of local compressions and extensions in response to the shear experiments carried on the considered heterogeneous fractured rock samples shown in Fig. 4.

3 CONCLUSIONS

Mesoscale fractures can generate important levels of both P- and S-wave attenuation due to WIFF between the fractures and the embedding porous matrix. When these fractures intersect, the attenuation behavior of both P- and S-waves changes dramatically compared to the corresponding unconnected scenario. In this presence of fracture connectivity, we observe a decrease in the attenuation peaks related to the unconnected scenarios together with the emergence of an additional prominent attenuation peak at higher frequencies. Our numerical simulations demonstrate that this additional manifestation of WIFF is mainly produced by fluid flow within the connected fractures, from one fracture into the other one.

Since all fractured media have a certain degree of interconnectivity, this additional manifestation of WIFF should be accounted in order to model realistic seismic wave propagation for such scenarios. Moreover, given that this attenuation mechanism contains critical hydraulic information with regard to the fractured rock, a deeper understanding of the evidence presented in this study may open a potential avenue for extracting this information from seismic data. Such efforts should include not only further numerical analyses to better understand the role played by the various parameters controlling seismic wave propagation in fractured media, but also corresponding laboratory experiments.

REFERENCES CITED

Bakulin, A., Grechka, V., Tsvankin, I., 2000. Estimation of Fracture Parameters from Reflection Seismic Data—Part I: HTI Model due to a Single Fracture Set. *Geophysics*, 65(6): 1788–1802. doi:10.1190/1.1444863

Berkowitz, B., Bour, O., Davy, P., et al., 2000. Scaling of Fracture Connectivity in Geological Formations. *Geophysical Research Letters*, 27(14): 2061–2064. doi:10.1029/1999gl011241

Berryman, J. G., Wang, H. F., 2001. Dispersion in Poroelastic Systems. *Physical Review E*, 64(1): 011303. doi:10.1103/physreve.64.011303

Biot, M. A., 1941. General Theory of Three-Dimensional Consolidation. *Journal of Applied Physics*, 12(2): 155–164. doi:10.1063/1.1712886

Biot, M. A., 1962. Mechanics of Deformation and Acoustic Propagation in Porous Media. *Journal of Applied Physics*, 33(4): 1482–1498. doi:10.1063/1.1728759

Brajanovski, M., Gurevich, B., Schoenberg, M., 2005. A Model for P-wave Attenuation and Dispersion in a Porous Medium Permeated by Aligned Fractures. *Geophysical Journal International*, 163(1): 372–384. doi:10.1111/j.1365-246x.2005.02722.x

Chapman, M., 2003. Frequency-Dependent Anisotropy due to Meso-Scale Fractures in the Presence of Equant Porosity. *Geophysical Prospecting*, 51(5): 369–379. doi:10.1046/j.1365-2478.2003.00384.x

Clark, R. A., Benson, P. M., Carter, A. J., et al., 2009. Anisotropic P-Wave Attenuation Measured from a Multi-Azimuth Surface Seismic Reflection Survey. *Geophysical Prospecting*, 57(5): 835–845. doi:10.1111/j.1365-2478.2008.00772.x

Holliger, K., Bühnemann, J., 1996. Attenuation of Broad-Band (50–1 500 Hz) Seismic Waves in Granitic Rocks near the Earth' Surface. *Geophysical Research Letters*, 23(15): 1981–1984. doi:10.1029/96gl01855

Jänicke, R., Quintal, B., Steeb, H., 2015. Numerical Homogenization of Mesoscopic Loss in Poroelastic Media. *European Journal of Mechanics-A/Solids*, 49: 382–395. doi:10.1016/j.euromechsol.2014.08.011

Maultzsch, S., Chapman, M., Liu, E. R., et al., 2003. Modelling Frequency-Dependent Seismic Anisotropy in Fluid-Saturated Rock with Aligned Fractures: Implication of Fracture Size Estimation from Anisotropic Measurements. *Geophysical Prospecting*, 51(5): 381–392. doi:10.1046/j.1365-2478.2003.00386.x

Nakagawa, S., Schoenberg, M. A., 2007. Poroelastic Modeling of Seismic Boundary Conditions across a Fracture. *The Journal of the Acoustical Society of America*, 122(2): 831–847. doi:10.1121/1.2747206

Nelson, R., 2001. Geologic Analysis of Naturally Fractured Reservoirs (2nd Ed.). Gulf Professional Publishing, Woburn. 332

Peacock, S., McCann, C., Sothcott, J., et al., 1994. Experimental Measurements of Seismic Attenuation in Microfractured Sedimentary Rock. *Geophysics*, 59(9): 1342–1351. doi:10.1190/1.1443693

Quintal, B., Steeb, H., Frehner, M., et al., 2011. Quasi-Static Finite Element Modeling of Seismic Attenuation and Dispersion due to Wave-Induced Fluid Flow in Poroelastic Media. *Journal of Geophysical Research*, 116(B1): B01201. doi:10.1029/2010jb007475

Quintal, B., Steeb, H., Frehner, M., et al., 2012. Pore Fluid Effects on S-Wave Attenuation Caused by Wave-Induced Fluid Flow. *Geophysics*, 77(3): L13–L23. doi:10.1190/geo2011-0233.1

Quintal, B., Jänicke, R., Rubino, J. G., et al., 2014. Sensitivity of S-Wave Attenuation to the Connectivity of Fractures in Fluid-Saturated Rocks. *Geophysics*, 79(5): WB15–WB24. doi:10.1190/geo2013-0409.1

Rubino, J. G., Ravazzoli, C. L., Santos, J. E., 2009. Equivalent Viscoelastic Solids for Heterogeneous Fluid-Saturated Porous Rocks. *Geophysics*, 74(1): N1–N13. doi:10.1190/1.3008544

Rubino, J. G., Guarracino, L., Müller, T. M., et al., 2013. Do Seismic Waves Sense Fracture Connectivity? *Geophysical Research Letters*, 40(4): 692–696. doi:10.1002/grl.50127

Rubino, J. G., Müller, T. M., Guarracino, L., et al., 2014. Seismoacoustic Signatures of Fracture Connectivity. *Journal of Geophysical Research: Solid Earth*, 119(3): 2252–2271. doi:10.1002/2013jb010567